Potential Intensification Rate of Tropical Cyclones in a Simplified Energetically Based Dynamical System Model: An Observational Analysis

Jing Xu[1], and Yuqing Wang[2*]

[1]State Key Laboratory of Severe Weather, Chinese Academy of Meteorological Sciences, China Meteorological Administration, Beijing, China

[2]International Pacific Research Center and Department of Atmospheric Sciences, University of Hawaii at Mānoa, Honolulu, HI 96822

August 6, 2021 (submitted)
November 20, 2021 (revised)
Dateline

Submitted to ***Journal of the Atmospheric Sciences***

Corresponding author: Prof. Yuqing Wang
Room 404A, IPRC/SOEST
University of Hawaii at Manoa
1680 East-West Road
Honolulu, HI 96822
Email: yuqing@hawaii.edu

Abstract

In a recent study by Wang et al. (2021a) that introduced a dynamical efficiency to the intensification potential of a tropical cyclone (TC) system, a simplified energetically based dynamical system (EBDS) model was shown to be able to capture the intensity-dependence of TC potential intensification rate (PIR) in both idealized numerical simulations and observations. Although the EBDS model can capture the intensity-dependence of TC intensification as in observations, a detailed evaluation has not yet been done. This study provides an evaluation of the EBDS model in reproducing the intensity-dependent feature of the observed TC PIR based on the best-track data for TCs over the North Atlantic, central, eastern and western North Pacific during 1982–2019. Results show that the theoretical PIR estimated by the EBDS model can capture basic features of the observed PIR reasonably well. The TC PIR in the best-track data increases with increasing relative TC intensity (intensity normalized by its corresponding maximum potential intensity–MPI) and reaches a maximum at an intermediate relative intensity around 0.6, and then decreases with increasing relative intensity to zero as the TC approaches its MPI, as in idealized numerical simulations. Results also show that the PIR for a given relative intensity increases with the increasing MPI and thus increasing sea surface temperature, which is also consistent with the theoretical PIR implied by the EBDS model. In addition, future directions to include environmental effects and make the EBDS model applicable to predict intensity change of real TCs are also discussed.

1. Introduction

Under the assumption of a tropical cyclone (TC) as a natural Carnot heat engine, there exists an upper limit of the TC intensity, namely, the maximum potential intensity (MPI) a TC may reach given favorable atmospheric and oceanic thermodynamic conditions (Emanuel 1986, 1991, 1997). Similarly, recent observational and theoretical studies have shown that there also exists a maximum potential intensification rate (MPIR) for an intensifying TC, i.e., the upper-limit of intensification rate (IR) a TC can attain given favorable thermodynamic environmental conditions (Xu et al. 2016; Xu and Wang 2018a). The MPIR has been shown to occur at an intermediate TC intensity in observations. Based on the TC best-track dataset during 1988–2014 in the North Atlantic, Xu et al. (2016) statistically analyzed the relationship between the TC MPIR and the underlying sea surface temperature (SST) and found a functional dependence of the MPIR on SST, similar with that of MPI. A similar empirical functional dependence of the MPIR on SST was also found for TCs over the western North Pacific (Xu and Wang 2018a).

Observations show that the TC intensification rate (IR), in particular the maximum IR for a given intensity (we refer to this as the potential IR or simply PIR), increases with TC intensity, reaches a maximum (namely, MPIR) when the TC is at its intermediate intensity with the 10-m sustained maximum wind speed (Vmax) of about 30-40 m s^{-1} (Kaplan et al. 2010; Xu et al. 2016; Xu and Wang 2015, 2018a), and then decreases to zero as Vmax further increases to approach its MPI. Kaplan et al. (2010) qualitatively explained this intensity-dependence of TC IR by a hypothesis that TCs are likely to intensify rapidly when its eyewall is well developed with strong organized convection but still far from their MPI, while afterwards, the IR tends to slow down when the intensity of the intensifying TC is getting close to its MPI, with the enhanced heating efficiency is mostly offset by the surface frictional dissipation effect. Xu et al. (2016) and Xu and Wang (2018a) argued that the initial increase in PIR with increasing TC intensity can be explained by the quasi-balanced dynamics, which predicts an increase of heating efficiency of eyewall convection with increasing inner-core inertial stability, which is a function of the TC intensity and inner-core size (Schubert and Hack, 1982; Vigh and Schubert 2009; Pendergrass and Willoughby 2009).

Previous studies on TC intensification mechanisms are all qualitative based on some positive feedback processes (see a review by Montgomery and Smith 2014). Recent studies have attempted to quantify TC PIR based on various assumptions and/or approximations. Two such efforts have been made to develop the time-dependent theories of TC intensification (Emanuel 2012; Ozawa and Shimokawa 2015). Emanuel (2012) started with the boundary layer entropy budget equation, assumed an axisymmetric vortex in thermal wind balance with neutral slantwise moist convection in the outwardly sloping eyewall, and derived an equation for the rate of change in TC intensity in terms of maximum tangential wind speed. The other time-dependent theory of TC intensification was developed by Ozawa and Shimokawa (2015), which views a TC as a Carnot heat engine and assumes that the TC intensifies, as measured by the increasing rate in the inner-core mechanical energy, when the energy production rate due to surface enthalpy flux is greater than the surface frictional dissipation rate (Wang 2012, 2015). Although based on different assumptions/approximations, both theories result in similar mathematical expressions for TC IR and predict IR to maximal at zero azimuthal velocity and decreasing with increasing TC intensity. This is not consistent with the observed intensity-dependence of TC IR as mentioned above (Xu et al. 2016; Xu and Wang 2015, 2018a). As also recently questioned by Montgomery and Smith (2019), it is unclear how a storm could intensify from a quiescent state because the surface enthalpy flux would be negligible as the TC maximum near-surface wind speed is close to zero, and thus supposedly no sufficient energy supply to initiate the intensification.

Recently, Wang et al. (2021a, hereafter W21a) indicated that the unrealistic intensity-dependence of TC IR in the theory of Ozawa and Shimokawa (2015) results mainly from the assumption of a constant efficiency for the transfer of the production rate of potential energy to the production rate of the inner-core mechanical kinetic energy. They introduced a dynamical efficiency to the TC system and developed a simplified energetically based dynamical system (EBDS) model to quantify the intensity-dependence of TC IR. According to this EBDS model, the TC IR is determined by the net increasing rate in the inner-core mechanical energy, which is the difference between the intensification potential due to the energy production rate and the weakening potential due to surface frictional dissipation under the eyewall. The intensification potential is a function of the thermodynamic conditions of the environment and the dynamical efficiency (E) of the TC system. The E depends strongly on the degree of convective organization within the eyewall and the inner-core inertial stability of the TC vortex. Unlike previous time-dependent theories that include mainly the environmental conditions (DeMaria 2009; Emanuel 2012; Ozawa and Shimokawa 2015; Emanuel and Zhang 2017), the new EBDS model includes the TC intrinsic dynamical efficiency determined by the inner-core inertial stability in the time-dependent theory of TC intensification. W21a showed that with the introduced an *ad-hoc* (intrinsic) dynamical efficiency, the EBDS model can quantitatively reproduce the TC IR in idealized numerical simulations and capture the basic features of the observed time-dependence of TC IR as mentioned above. More recently, Wang et al. (2021b, hereafter W21b) developed a new time-dependent theory of TC intensification based on the tangential wind budget equation and assumed a thermodynamic quasi-equilibrium in the slab TC boundary layer. By introducing an *ad-hoc* intensity-dependent parameter to measure the extent to which the absolute angular momentum and the moist entropy surfaces are congruent, W21b derived an equation for the TC IR, which has the same mathematical form as the one obtained in W21a but with a different physical interpretation for the parameter equivalent to the dynamical efficiency in the EBDS model. There are two main differences in the theories between W21b and Emanuel (2012). First, W21b did not assume the radius of maximum wind being a material surface, namely the absolute angular momentum following the RMW is not conserved, which was an unrealistic assumption used in Emanuel (2012). Second, in W21b the congruent assumption between the entropy and absolute angular momentum surfaces (namely the moist neutral eyewall ascent) in Emanuel (2012) is removed since later studies have demonstrated that the moist neutral slantwise assumption is actually not hold during the intensification rate, only at the mature stage (Peng et al. 2018; Kieu et al. 2020).

In both W21a and W21b, the new time-dependent equation for TC IR was carefully evaluated using idealized ensemble full-physics model simulations with a nonhydrostatic, convection-resolving model. They showed that the simulated TC IR initially increases with the relative TC intensity (namely, the TC intensity normalized by its MPI) and reaches a maximum at an intermediate relative intensity, and then decreases with increasing relative intensity to zero as the TC approaches its MPI, as in observations. W21b also found that for a given relative intensity, the TC IR increases with the square of its MPI. Since no environmental flow was included in their idealized simulations, the IR of the modeled TCs can be considered as the PIR, which is governed primarily by the internal dynamics under the given favorable thermodynamic conditions, such as the realistic environmental atmospheric soundings and SSTs. Although the EBDS model was shown to be able to qualitatively capture the overall intensity-dependence of the observed TC PIR as briefly mentioned in both W21a and W21b, a detailed comparison between the PIRs of the EBDS model and those of the observed TCs has not yet been done. This study attempts to validate and evaluate the EBDS model using the best-track data for TCs over the main TC basins (North Atlantic, central, eastern and western North Pacific) in the Northern Hemisphere. We will show that the calibrated intrinsic dynamical efficiency based on idealized numerical simulations is supported by observations, and the EBDS model can well reproduce the basic features of the observed PIR of TCs. The rest of the paper is organized as follows. Section 2 briefly describes the data and the analysis methods. The EBDS model is briefly reviewed in section 3. The basic features of TC PIR obtained from the best-track TC data are discussed and compared with the theoretical PIR obtained from the EBDS model in section 4. Major conclusions are drawn in the last section.

2. Data and methodology

The statistical hurricane intensity prediction scheme (SHIPS) dataset (Knaff et al, 2005; updated on April 3, 2020) is used in this study. All best-track data of TCs over the main basins of the Northern Hemisphere, including all TCs over the North Atlantic, the central and eastern North Pacific during 1982–2019 and those over the western North Pacific during 1990–2017, are considered in our analysis. The 6-hourly maximum sustained 10-m wind speed, Reynolds SST, and the Emanuel's maximum potential intensity (MPI) are all adopted from the SHIPS dataset. The MPI and other environmental variables in the SHIPS dataset are estimated using the operational synoptic datasets (DeMaria and Kaplan 1999; Knaff et al. 2005), which are derived from the Climate Forecast System Reanalysis (CFSR) reanalysis dataset. To minimize the influence of TC translation on its intensity, the 40% of the TC translation speed was subtracted from the initial maximum wind speed for all TC cases, and the result is used as the measure of TC intensity (Vmax), as done by Emanuel et al. (2004). The TC intensity changes at 6-h intervals are calculated accordingly ($IR_{6h} = V_{max}^{t+6h} - V_{max}^{t}$). Only the intensification cases ($IR_{6h} > 0$) with Vmax greater than 17 m s^{-1} are included in our analysis. TCs in SHIPS dataset with missing values for SSTs and MPIs are removed to avoid the landfalling TCs. Only TCs with tropical nature and with SST greater than 25℃ and south of 35°N are considered in our analysis to avoid extratropical transition stages. The time period and corresponding numbers of TCs and intensification cases in individual basins included in this study are summarized in Table 1.

Although the MPI can reasonably capture the observed TC maximum intensity, it still understates the observed maximum intensity of some TCs. Those cases are often termed as superintensity (e.g., Persing and Montgomery 2003; Montgomery et al. 2006; Wang and Xu 2010; Rousseau-Rizzi and Emanuel 2019; Li et al. 2020). The superintensity will cause negative IR for those intensifying TC cases according to the IR equations (see Eq.17 in Emanuel 2012; Eq. 12 in W21a; Eq. 16 in W21b). To avoid such unrealistic situations, W21a and W21b used the steady-state intensity of the simulated TCs instead of the theoretical MPI in their time-dependent theory of TC intensification. The steady-state intensity of the simulated TC in both W21a and W21b refers to the maximum intensity attained in the quasi-steady state in an idealized simulation, while the theoretical MPI for a real TC is estimated by using the actual atmospheric sounding under a given SST and the environmental atmospheric soundings. Based on the diagnostic results of Wang and Xu (2010) and Li et al. (2020) and the theoretical work of Kowaleski and Evans (2016), the superintensity resulted from the ignorance of any possible inward transport of energy production due to enthalpy flux from the underlying ocean outside the RMW in the classic MPI theory (Emanuel 1997). Wang and Xu (2010) demonstrated that the inward transport of energy production from the outside of the RMW can be an extra energy source (25%) to balance the power dissipation due to surface friction under the eyewall. Wang and Xu (2010) showed that this extra energy source can lead to an 11.2% increase of the estimated MPI. Li et al. (2020) also showed that the quasi-steady state intensity of the simulated TCs can be 7%~18% greater than their theoretical MPI in idealized simulations with realistic tropical environmental conditions. Note that some other studies have attributed the TC superintensity to the unbalanced flow in the boundary layer (Bryan and Rotunno 2009; Frisius et al. 2013) In the SHIPS dataset, we found that there are 166 superintensity cases out of 11758 intensifying cases with their intensities exceeding 11% of their MPIs, which is within the range of the simulated TCs in Li et al. (2020). We therefore simply multiplied the SHIPS MPI by a factor of 1.11 to take into account of the superintensity nature of TCs. After such a modification, all TC MPIs are greater than or equal to their intensities, and thus there is no negative theoretical IR for any intensifying TCs in our analysis.

We should mention here that uncertainties in the estimated MPI and also the best-track TC intensity exist and are unavoidable. For example, the estimated MPI depends on the definition of the environmental thermodynamic conditions (e.g., Xu et al. 2019a,b). The surface drag coefficient in the theoretical MPI is currently treated to be independent of the near-surface wind speed while it is a strong function of the near-surface wind speed (e.g., Donelan et al. 2004; Soloviev et al. 2017; Donelan 2018). The estimated best-track maximum wind speed varies as a result of the storm intensity and the available observations and may not well-represent the storm-scale intensity (Landsea and Franklin 2013). Therefore, some constraints used in modifying the SHPIS MPIs and the occurrences of some small TC cases that show the theoretically estimated PIR underestimates the maximum IR in the best-track data should be considered necessary and acceptable. Nevertheless, our results seem to strongly suggest that the use of TC MPIs from the SHIPS dataset with the modification to take into account of the possible superintensity nature is acceptable for the purpose of this study. Actually, we will show that the theoretically estimated PIR using the SHIPS MPI and best-track TC intensity well captures the maximum IR calculated using the best-track TC intensity, suggesting that some uncertainties in the data used in this study should not be a big issue with some constraints as mentioned above.

3. An overview of the EBDS model of TC intensification

The EBDS model developed in W21a is a time-dependent equation for the IR of a TC given its current intensity V_{max} and the corresponding MPI (V_{mpi})

$$\frac{\partial V_{max}}{\partial \tau} = \frac{C_D}{H}\left(EV_{mpi}^2 - V_{max}^2\right). \tag{1}$$

where $\frac{\partial V_{max}}{\partial \tau}$ is the rate of TC intensity change, V_{max} is the time-dependent near-surface maximum wind speed (referred to as intensity) of the TC, V_{mpi} is the corresponding MPI as discussed in section 2, which partly includes the contribution of superintensity, C_D is surface drag coefficient, H is an undetermined height parameter, which is roughly twice the depth of the boundary layer (Emanuel 2012)[1]. In W21a and W21b, C_D was taken directly from their idealized numerical simulations and the MPI was taken from the steady-state intensity, which includes the superintensity component. They found that $H = 2000\ m$ gives the best fit of the theoretical IR to the TC IR in their idealized simulations. Although C_D and H are two independent parameters in the EBDS model, C_D/H can be considered as one parameter in practice since neither of C_D nor H can be accurately determined from observations. Nevertheless, after many tests based on the best-track TC data described above, we found that $H = 2000\ m$ and $C_D = 2.4 \times 10^{-3}$ are the

[1] Note that $H = 2h$ in Emanuel (2012) with h being the boundary layer depth near the radius of maximum wind. In previous studies, various values have been used for h, e.g., 5,000 m in Emanuel (2012); 4,000 m (with H=8,000 m) in Ozawa and Shimokawa (2015); 1,400 m in Emanuel and Zhang (2017) and Emanuel (2017) with $C_D = 1.2 \times 10^{-3}$. Observations suggest that the characteristic height scale of the TC inner-core boundary layer is usually between 500–2000 m (Zhang et al. 2011), the reasonable height parameter H can be considered to be between ~1000–4000 m. W21a and W21b found that the predicted IR using the EBDS model with H = 2,000 m fits well the IR of their simulated TCs.

best choice and thus will be used in our following analysis. Actually, both are quite reasonable under TC conditions (e.g., Donelan et al. 2004; Zhang et al. 2011). This implies that several key parameters used in the EBDS model calibrated using idealized full-physics model simulations discussed in W21a or the new time-dependent theory of TC intensification developed in W21b are applicable to real TCs. We will show in the next section that the EBDS model with the above-mentioned values of C_D and H can provide quite good estimation of PIR of TCs in observations. The dynamical efficiency E ($0 \leq E \leq 1$) in Eq. (1) reflects the effective conversion of potential energy production to kinetic energy production for the TC system. The first term on the right-hand side of Eq. (1) represents the intensification potential of a TC, and the second term is the weakening potential due to surface frictional effect. Note that the TC genesis in nature is related to many other processes that have not been considered in the EBDS model. That is, some assumptions made in deriving the new IR equation are not relevant to TC genesis in nature, such as the axisymmetric structure with favorable environmental conditions.

Different from TCs in idealized simulations in which no unfavorable environmental factors were included, a real TC is always embedded in an environmental flow and may be affected by various unfavorable environmental conditions, such as the large-scale vertical wind shear and the negative feedback associated with cooling due to upwelling and mixing in the upper ocean induced by the TC itself. Since these effects play a role in deterring TC intensification, it is not unrealistic to assume that the dynamical efficiency E determined by the storm-scale dynamics (or simply the intrinsic dynamical efficiency) would be reduced by a fraction (E') due to all possible inhibiting environmental effects. This means that we can simply rewrite E in Eq. (1) as

$$E = E^* \times E', \tag{2}$$

where E^* is the intrinsic dynamical efficiency of the TC system, and E' is the environmental dynamical efficiency measuring all inhibiting environmental effects on TC intensification. By definition, E' should be less than 1 and greater than 0, similar to E^*. In this sense, the case of $E' = 1$ and thus $E = E^*$ means that an intensifying TC can reach its PIR given all favorable environmental conditions.

For a given TC, E in Eq. (1) can be calculated using the observed IR ($\frac{\partial V_{max}}{\partial \tau}$) and intensity V_{max} with the corresponding V_{mpi} if C_D/H is also given. We can assume that the intrinsic dynamical efficiency $E*$ should be comparable to the maximum E for a given relative intensity (V_{max}/V_{mpi}) and the corresponding MPI (V_{pmi}). In this sense, the theoretical IR should be comparable to the observed maximum IR, or PIR by definition. Since the main objective of this study is to evaluate the EBDS model using observations, we will focus on the theoretically estimated PIR using the best-track TC data and other available data as mentioned in section 2. Note that the theoretical PIR is obtained based on several key assumptions as mentioned in section 1. $V_{\max}$ in Eq. (6) should be referred to the near-surface azimuthal mean wind speed. However, the real TCs may include asymmetric structure and the estimated best-track intensity may partly contributed by the asymmetric structure of the TC even on the storm scale (Landsea et al. 2017). Although we have minimized the possible contribution by subtracting 40% of the storm translation speed (Emanuel 2004), the internally generated or environmentally forced asymmetries in the storm are neither included in the theory nor considered in our analysis. Our results seem to suggest that in terms of the PIR, the effect of asymmetric structure is secondary and thus will be discussed in our following discussion.

The intrinsic dynamical efficiency E^* introduced by W21a is a function of the inner-core inertial stability (I) normalized by the inertial stability of the TC at its mature stage with MPI (I_{mpi}), namely

$$E^* = \left(\frac{I}{I_{mpi}}\right)^n = \left[\frac{\sqrt{\left(f+\frac{2V}{r}\right)\left(f+\frac{\partial rV}{r\partial r}\right)|_{rm}}}{\sqrt{\left(f+\frac{2V}{r}\right)\left(f+\frac{\partial rV}{r\partial r}\right)|_{rmpi}^{mpi}}}\right]^n, \tag{3}$$

where r_m is RMW of the intensifying TC and r_{mpi} is the RMW of the TC at its mature stage of MPI. The power constant n =1.0 is found to provide the best fit of the theoretical IR predicted by Eq. (1) with the IR of the simulated TCs in W21a. For the simplest case, assuming both the r_m and the Coriolis parameter (f) are not too large, we can assume that the TC eye region is in solid body rotation and Eq. (3) with $n = 1.0$ can be approximated as

$$E^* \cong \left(\frac{f+\frac{2V_{max}}{r_m}}{f+\frac{2V_{mpi}}{r_{mpi}}}\right) \cong \frac{V_{max}}{V_{mpi}} \times \frac{r_{mpi}}{r_m}, \tag{4}$$

Although r_m of a TC at a given time is available in the best-track data, r_{mpi} of the corresponding MPI is unknown. Considering the fact that a TC intensifies with the contraction of the RMW (Li et al. 2019; 2021), we can parameterize the RMW ratio in Eq. (4) as a function of the relative intensity as well, and thus we can rewrite Eq. (4) as

$$E^* \cong \left(\frac{V_{max}}{V_{mpi}}\right)^m, \tag{5}$$

where m is a power constant and can be calibrated using results from idealized full-physics numerical simulations or observations. W21b found that $m = 3/2$ gives the best fit of the estimated theoretical PIR to the IR of TCs in idealized numerical simulations. We will show in the next section that $m = 3/2$ is also the best choice for the PIR of the observed TCs. Substituting (2) and (5) into Eq. (1), we have

$$\frac{\partial V_{max}}{\partial \tau} = \frac{C_D}{H} V_{mpi}^2 \left[E' \left(\frac{V_{max}}{V_{mpi}} \right)^m - \left(\frac{V_{max}}{V_{mpi}} \right)^2 \right]. \quad (6)$$

Equation (6) has the same form as Eq. (23) in W21b if *E'* here is replaced by *B* in W21b and $m = 3/2$ is taken. As mentioned earlier, this study focuses on the PIR of a given TC at a given time, we thus intentionally take $E' = 1.0$ in the following analysis. As a result, three parameters are needed to be given to determine the PIR of a TC at a given time; they are the surface drag coefficient C_D, the boundary layer depth H, and the MPI if m is calibrated based on the best-track TC data.

4. Evaluation of the EBDS model against observations

a. The intrinsic dynamical efficiency (E^*)

Figure 1a shows the calculated dynamical efficiency (E) in Eq. (1) using the 6-h best-track TC data in section 2 and other parameters discussed in section 3 versus the relative intensity. We can see that the power constant $m = 3/2$ in Eq. (5) gives the best fit of the upper-limit of E, which corresponds to the intrinsic dynamical efficiency (E^*). With $m = 3/2$, Eq. (1) or (6) will become the same as the IR equation derived in the new time-dependent theory of TC intensification in W21b. For a comparison, we also give the results for $m = 1.0$ and $m = 1.2$ in Fig. 1a. For those smaller m, E^* is overestimated, resulting in too large theoretical PIR (Figs. 1b and 1c). With $m = 3/2$, the PIR provides good quantitative estimate of the observed maximum IR although some of the observed maximum IRs (about 0.6% cases) are underestimated (Fig. 1d) because the intrinsic dynamical efficiency E^* for some intensification cases could be underestimated (Fig. 1a). We checked the cases with the underestimated PIR and found that the occurrences are likely random (not shown). Such a small underestimation is acceptable considering the fact that the EBDS model only includes several key parameters, while it still can capture the major features of the intensity-dependencies of both the intrinsic dynamical efficiency and the PIR of TCs in observations.

The above results demonstrate that the intrinsic dynamical efficiency can be defined as a function of the relative intensity, with which the EBDS model has skills in capturing the PIR of the observed TCs. It is also important to see the characteristics of the remaining component of the dynamical efficiency E' in Eq. (2) or (6), which measures all inhibiting environmental effects on TC intensification, or termed the environmental dynamical efficiency. Figure 2 shows the dependences of E', which is calculated by E/E^* [see Eq. (2) above], on the relative intensity and the normalized IR (namely IR normalized by the corresponding theoretical PIR at a given time). We can see that overall E' is less than 1.0 but greater than 0.5, with high density at 0.6–0.7, suggesting that the environmental factors may slow down the TC intensification, and the PIR of an intensifying TC is determined primarily by the TC internal dynamics given favorable environmental thermodynamic conditions. In general, E' increases with increasing TC relative intensity (Fig. 2a). This indicates that TCs that approach their MPI correspond to higher dynamical efficiency with favorable environmental conditions and/or are potentially more resistant to unfavorable environmental conditions. From Fig. 2b, we can see that although E'

also shows a general tendency to increase with increasing normalized IR as with increasing relative intensity, the dependence on the former is relatively weaker than on the latter. Particularly, the high-density dots in Fig. 2b indicate that the slowly intensifying TC (with the normalized IR less than 0.4) is largely due to the inhibiting effect of unfavorable environmental factors, or equivalently, TCs embedded in favorable environment can intensify more rapidly. An effort on determining the environmental factors that contribute to the environmental dynamical efficiency *E'* is under way and the results will be reported in due course. Nevertheless, the above analyses further imply that the intrinsic dynamical efficiency determined and discussed above is reasonable.

b. Comparison of PIR in the EBDS model with observations

Based on the parameter settings as mentioned above, we can calculate the theoretical PIR for all intensifying TCs at 6-h intervals using Eq. (6) and compare it with the corresponding maximum IR calculated based on the best-track data. Figure 3 compares the distributions of the theoretical PIR and the 99th percentile of IRs from observations in the phase spaces of V_{max}–V_{mpi} and relative intensity (V_{max}/V_{mpi})–V_{mpi}, respectively. The 99th percentile of IRs is used to represent the maximum IR (IRmax) under favorable environmental conditions for a relatively fair comparison with the theoretical PIR estimated from the EBDS model. It is clear that the theoretical PIR increases with increasing MPI monotonously, while for a given MPI it increases with TC intensity initially and reaches the maximum at an immediate intensity, and then decreases with increasing TC intensity (Fig. 3a). This dependence can be more explicitly seen from the phase space in relative intensity (V_{max}/V_{mpi})–V_{mpi}. Note that the maximum PIR (MPIR) increases with increasing MPI [actually the square of MPI as inferred from Eq. (6)] and occurs when the relative intensity is between 0.5-0.6 (Fig. 3b). The observed IRmax (Figs. 3c and 3d) shows very similar distributions as the theoretically estimated PIR in the phase spaces of TC intensity/relative intensity and V_{mpi}. This demonstrates that the EBDS model is well supported by observations. Namely, with the introduced intrinsic dynamical efficiency, the EBDS model can reasonably capture the upper-limit of the observed TC IR and its dependence on TC intensity and its corresponding MPI. Note that at relatively lower MPIs, IRmax occurs at higher relative intensity side (Fig. 3d). This might be due to the fact that C_D often increases with increasing TC intensity when the TC is weak (Donelan et al. 2004). This can explain the shift of IRmax to the high relative intensity side for weak TCs.

It is our interest to further examine the major features of the observed TC IR, including its dependence on TC intensity and the underlying SST and see whether the EBDS model can capture these features. Figure 4 shows the observed IR and the corresponding theoretical PIR estimated using Eq. (6), respectively, against TC intensity in different SST bins. For each SST bin, the upper limit of the theoretical PIR, namely the 99th percentile of PIR, increases with increasing TC intensity before V_{max} reaches an intermediate intensity as implied in Fig. 3a, which is consistent with the idealized simulations in W21a and W21b. The theoretical PIR captures well the upper limits of TC IRs in all SST bins, suggesting that the EBDS model can well define the PIR of observed TCs. The theoretical MPIR in each SST bin increases with increasing SST and occurs at the relative intensity of around 0.5–0.6 (Fig. 4f). For example, the MPIR is about

15 m s^{-1} $(6h)^{-1}$ when SST is below 26.5℃, and increases to about 25 m s^{-1} $(6h)^{-1}$ when SST is greater than 29.5℃ (Fig. 4f).

Since the theoretical PIR is determined by two processes (terms): the intensification potential ($\frac{C_D}{H}E^*V_{mpi}^2$) and the frictional weakening potential ($\frac{C_D}{H}V_{max}^2$) as given in Eq. (1), it is our interest to further examine the dependence of the two terms on TC relative intensity in each SST bin in observations. The intensity-dependent intensification potential and frictional weakening potential against relative intensity in each SST bins are compared in Fig. 5. It is clear that with the introduced intrinsic dynamical efficiency E*, the median of the intensification potential increases almost linearly with increasing relative intensity for each SST bin, while the frictional weakening potential increases quadratically with increasing relative intensity. As a result, both terms are relatively small when a TC is weak, giving rise to a relatively small IR. As the TC intensifies, the frictional weakening potential increases with relative intensity slower than the intensification potential, corresponding to the increase of IR with increasing relative intensity. After the TC attains an intermediate relative intensity, the frictional weakening potential increases with increasing relative intensity faster than the intensification potential. As a result, the IR reaches a maximum at some intermediate relative intensity, and then decreases with increasing relative intensity, and approaches zero when the TC reaches its MPI. This demonstrates that the intensity-dependence of PIR in the EBDS model is well supported by observations. In addition, as we can see from Eq. (6) with $m = 3/2$, the IR is proportional to the square of the corresponding MPI for a given relative intensity, which can also be implied by the fact that the slopes of both intensification potential and frictional weakening potential increase with increasing SST (or the corresponding MPI) in Fig. 5f.

5. Conclusions and discussion

In a recent study, W21a introduced a dynamical efficiency to the intensification potential of a TC system in a simplified EBDS model and showed that the modified EBDS model can reproduce the intensity-dependence of TC potential intensification rate (PIR) in idealized numerical simulations. Although they also briefly indicated that the EBDS model can capture the overall intensity-dependence of PIR in observations, such as those documented in Xu et al. (2016) and Xu and Wang (2015, 2018a), they did not perform any detailed evaluation. In this study, the EBDS model's capability in capturing the basic features of the observed TC PIR has been evaluated based on the best-track TC data over the North Atlantic, central, eastern and western North Pacific during 1982–2019. Results first demonstrate that the intrinsic dynamical efficiency obtained based on the idealized numerical simulations in W21b is well supported by observations.

With the defined intrinsic dynamical efficiency, the EBDS model can reproduce well the observed intensity-dependence of the 99th percentile IRs in the best-track data over the North Atlantic, central, eastern and western North Pacific. Both the estimated theoretical PIR and the observed maximum IR initially increase with increasing TC relative intensity (intensity normalized by its corresponding MPI) and reach their maxima at an intermediate relative intensity of around 0.6, and then decrease with further increase in relative intensity and approach zero as the TC reaches its MPI. The increase in the theoretical PIR for a given relative intensity with increasing MPI is also well supported by observations. Results also show that the maximum PIR of 15 m s^{-1} $(6h)^{-1}$ for SST below 26.5°C increases to around 25 m s^{-1} $(6h)^{-1}$ for SST greater than 29.5°C. The consistency between the theoretical PIR and the observed maximum IRs strongly suggests that the EBDS model can reliably estimate the PIR of real TCs, which can be considered as an upper limit of the TC IR or used as a parameter in statistical TC intensity prediction schemes.

We have also shown that the modified EBDS model can explain well the observed intensity-dependent TC PIR. The PIR is determined by the difference between the intensification potential and the frictional weakening potential. In the initial intensifying stage when the TC is weak with small relative intensity, the intensification potential is larger than the frictional weakening potential but both are small, corresponding to relatively small PIR. As the TC intensifies, the increase in the frictional weakening potential with increasing relative intensity is slower than the increase in the intensification potential, leading to the increase of PIR with increasing relative intensity. After the TC intensifies to attain an intermediate relative intensity, the increase in the frictional weakening potential with increasing relative intensity is faster than the increase in the intensification potential, giving rise to a maximum PIR at some intermediate relative intensity. This is followed by a decrease of PIR with increasing relative intensity, and then the PIR approaches zero when the TC reaches its MPI.

With the intrinsic dynamical efficiency $E*$ that determines the PIR, the actual TC IR will be controlled by the environmental factors, which can be included as the environmental dynamical efficiency (E') in the EBDS model Eq. (6). We have shown that the environmental effects represented as the environmental dynamical efficiency ($0 \leq E' \leq 1$) suppress TC IR by reducing the intrinsic dynamical efficiency (E*). Note that since the detrimental environmental effects may lead to the weakening of a TC, E' should be quantified by the intensity change during the whole lifetime of a TC rather than the intensifying stage only. The weakening TC cases should be included in characterizing and quantifying the environmental dynamical efficiency, which could be a function of the environmental vertical wind shear, the TC translational speed, and so on. In our next step, we will quantify the environmental dynamical efficiency with not only the intensifying TC cases but also both quasi-steady and weakening TC cases based on the best-track TC data, the SHIPS dataset, and the global reanalysis data. Once the environmental dynamical efficiency is determined, the EBDS model may be used to estimate and predict real TC intensity change given the environmental parameters. In addition, Previous studies have shown that although the surface exchange coefficient (C_k) is almost independent of the near surface wind speed, the drag coefficient C_D depends strongly on the near surface wind speed and thus the TC intensity (Soloviev et al. 2017; Donelan 2018). A wind-dependent C_D could be used in the EBDS model. In that case, C_D in Eq. (6) will vary with TC intensity and the MPI should be recalculated since it is a function of C_D. This will be considered in our follow-up study when the model is further developed for the real-time TC intensity prediction. The results will be reported separately in due course.

Acknowledgments: This study was supported in part by National Natural Science Foundation of China under grants 41730960，41875057, 41875114 and in part by the National Key R&D

Program of China under grant 2017YFC1501602. Y. Wang was supported partly by NSF grant AGS-1834300. The SHIPS data are downloaded from https://rammb.cira.colostate.edu/research/tropical_cyclones/ships/developmental_data.asp.

References

Bister, M., and K. A. Emanuel, 1998: Dissipative heating and hurricane intensity. *Meteor. Atmos. Phys*., **80**, 131–164, doi:10.1007/BF01030791.

Bryan, G. H., and R. Rotunno, 2009: Evaluation of an analytical model for the maximum intensity of tropical cyclones. *J. Atmos. Sci.,* **66**, 3042–3060, doi:10.1175/2009JAS3038.1.

Carrasco, C., C. Landsea, and Y. Lin, 2014: The influence of tropical cyclone size on its intensification. *Wea. Forecasting*, **29,** 582–590, doi:10.1175/WAF-D-13-00092.1.

DeMaria, M. 2009: A simplified dynamical system for tropical cyclone intensity prediction. *Mon. Wea. Rev.*, **137**, 68–82, doi:10.1175/2008MWR2513.1.

DeMaria, M., and J. Kaplan, 1999: An updated statistical hurricane intensity prediction scheme (SHIPS) for the Atlantic and eastern north Pacific basins. *Wea. Forecasting*, **14**, 326–337, doi:10.1175/1520-0434(1999)014<0326:AUSHIP>2.0.CO;2.

Donelan, M. A., B. K. Haus, N. Reul, W. J. Plant, M. Stiassnie, H. C. Graber, O. B. Brown, and E. S. Saltzman, 2004: On the limiting aerodynamic roughness of the ocean in very strong winds. *Geophys. Res. Lett.*, **31**, L18306, doi:10.1029/ 2004GL019460.

Donelan, M. A., 2018: On the decrease of the oceanic drag coefficient in high winds. *J. Geophys. Res.: Oceans*, **123**, 1485–1501, doi: 10.1002/2017JC013394.

Emanuel, K. A., 1997: Some aspects of hurricane inner-core dynamics and energetics. *J. Atmos. Sci.*, **54**, 1014–1026, doi:10.1175/1520-0469(1997)054<1014:SAOHIC>2.0.CO;2.

Emanuel, K. A., 1986: An air–sea interaction theory for tropical cyclones. Part I: Steady-state maintenance. *J. Atmos. Sci*., **43**, 585–604, doi:10.1175/1520–0469(1986)043<0585:AASITF>2.0.CO;2.

Emanuel, K. A., 1991: The theory of hurricanes. *Annu. Rev. Fluid Mech*., **23**, 179–196, doi:10.1146/ANNUREV.FL.23.010191.001143.

Emanuel, K. A., 1997: Some aspects of hurricane inner-core dynamics and energetics. *J. Atmos. Sci*., **54**, 1014–1026, doi:10.1175/1520-0469(1997)054<1014:SAOHIC>2.0.CO;2.

Emanuel, K. A., C. DesAutels, C. Holloway, and R. Korty, 2004: Environmental control of tropical cyclone intensity. *J. Atmos. Sci*., **61**, 843–858, doi:10.1175/1520-

0469(2004)061,0843:ECOTCI.2.0.CO;2.

Emanuel, K. A., 2012: Self-stratification of tropical cyclone outflow: Part II: Implications to storm intensification. *J. Atmos. Sci.*, **69**, 988–996, doi:10.1175/JAS-D-11-0177.1.

Emanuel, K., 2017: A fast intensity simulator for tropical cyclone risk analysis. *Nat. Hazards*, **88**, 779–796, doi:10.1007/s11069-017-2890-7.

Emanuel, K. and F. Zhang, 2017: The Role of Inner-core moisture in tropical cyclone predictability and practical forecast skill. *J. Atmos. Sci.,* **74**, 2315–2324, doi:10.1175/JAS-D-17-0008.1.

Frisius, T., D. Schönemann, and J. Vigh, 2013: The impact of gradient wind imbalance on potential intensity of tropical cyclones in an unbalanced slab boundary layer model. *J. Atmos. Sci.*, **70**, 1874–1890, doi:10.1175/JAS-D-12-0160.1.

Knaff, J. A., C. R. Sampson, and M. DeMaria, 2005: An operational statistical typhoon intensity prediction scheme for the western North Pacific. *Wea. Forecasting,* **20**, 688–699, doi:10.1175/WAF863.1.

Knapp, K. R., & Kruk, M. C. 2010: Quantifying interagency differences in tropical cyclone best-track wind speed estimates. *Mon. Wea. Rev*., **138**, 1459–1473. https://doi:10.1175/2009MWR3123.1.

Kaplan, J., M. DeMaria, and J. A. Knaff, 2010: A revised tropical cyclone rapid intensification index for the Atlantic and eastern North Pacific basins. *Wea. Forecasting*, **25**, 220–241, doi: 10.1175/2009WAF2222280.1.

Kieu, C., R. Rotunno, and Q. Wang, 2020: Frictionally induced feedback in a reduced dynamical model of tropical cyclone intensification. *J. Atmos. Sci.*, **77**, 3821–3831, doi: 10.1175/JAS-D-20-0092.1.

Kowaleski, A. L., and J. L. Evans, 2016: A reformation of tropical cyclone potential intensity theory incorporating energy production along a radial trajectory. *Mon. Wea. Rev*., **144**, 3569–3578, DOI: 10.1175/MWR-D-15-0383.1.

Landsea, C. W., & Franklin, J. L. (2013). Atlantic hurricane database uncertainty and presentation of a new database format, *Mon. Wea. Rev.*, **141**, 3576–3592, doi:10.1175/MWR-D-12-00254.1.

Li, Y.-L., Y. Wang, and Y.-L. Lin, 2019: Revisiting the dynamics of eyewall contraction of tropical cyclones. *J. Atmos. Sci.*, **76**, 3229–3245, https://doi.org/10.1175/JAS-D-19-0076.1.

Li, Y., Y. Wang, Y. Lin, R. Fei, 2020: Dependence of superintensity of tropical cyclone on SST in axisymmetric numerical simulations. *Mon. Wea. Rev.*, **148**, 4767–4781, doi:10.1175/MWR-D-20-0141.1.

Li, Y.-L., Y. Wang, Y.-L. Lin, and X. Wang, 2021: Why does rapid contraction of the radius of maximum wind precede rapid intensification in tropical cyclones? *J. Atmos. Sci.*, **78**, 3441–3453, doi:10.1075/JAS-D-21-0129.1.

Montgomery, M. T., M. M. Bell, S. D. Aberson, and M. L. Black, 2006: Hurricane Isabel (2003): New insights into the physics of intense storms. Part I: Mean vortex structure and maximum intensity estimates. *Bull. Amer. Meteor. Soc*., **87**, 1335–1348, doi:10.1175/BAMS-87-10-1335.

Montgomery, M. T., and R. K. Smith, 2014: Paradigms for tropical cyclone intensification. *Aust. Meteor. Ocean.*, *(Bruce Morton Memorial Volume)*, **64**, 37–66, doi:10.22499/2.6401.005.

Montgomery, M. T., and R. K. Smith, 2019: Toward understanding the dynamics of spinup in Emanuel's tropical cyclone model. *J. Atmos. Sci*., **76**, 3089–3093, doi:10.1175/JAS-D-19-0051.1.

Ozawa, H., and S. Shimokawa, 2015: Thermodynamics of a tropical cyclone: generation and dissipation of mechanical energy in a self-driven convection system. *Tellus A*, **67**, 24216, doi:10.3402/tellusa.v67.24216.

Pendergrass, A. G., and H. E. Willoughby, 2009: Diabatically induced secondary flows in tropical cyclones. Part I: Quasi-steady forcing. *Mon. Wea. Rev.*, **137**, 805–821, doi:10.1175/2008MWR2657.1.

Peng, K., R. Rotunno, and G. H. Bryan, 2018: Evaluation of a time- dependent model for the intensification of tropical cyclones. *J. Atmos. Sci.*, **75**, 2125–2138, doi:10.1175/JAS-D-17-0382.1.

Persing, J., and M. T. Montgomery, 2003: Hurricane superintensity. *J. Atmos. Sci*., **60**, 2349–2371, doi:10.1175/1520-0469(2003)060<2349:HS>2.0.CO;2.

Rogers R., P. Reasor, and S. Lorsolo, 2013: Airborne doppler observations of the inner-core structural differences between intensifying and steady-state tropical cyclones. *Mon. Wea. Rev.,* **141**, 2970–2991, doi:10.1175/MWR-D-12-00357.1.

Rousseau-Rizzi, R., and K. Emanuel, 2019: An evaluation of hurricane superintensity in Axisymmetric Numerical Models. *J. Atmos. Sci.,* **76**, 1697–1706, doi:10.1175/JAS-D-18-0238.1.

Schubert W. H., and J. J. Hack, 1982: Inertial stability and tropical cyclone development. *J. Atmos. Sci.,* **39**, 1687–1697, doi:10.1175/1520-0469(1982)039<1687:ISATCD>2.0.CO;2.

Soloviev, A. V., R. Lukas, M. A. Donelan, B. K. Haus, and I. Ginis, 2017: Is the state of the air-sea interface a factor in rapid intensification and rapid decline of tropical cyclones? *J. Geophys. Res. – Oceans*, **122**, 10,174–10,183, doi: 10.1002/2017JC013435.

Stern, D. P., J. L. Vigh, D. S. Nolan, and F. Zhang, 2015: Revisiting the relationship between eyewall contraction and intensification. *J. Atmos. Sci*., **72**, 1283–1306, doi:10.1175/JAS-D-14-0261.1.

Vigh J. L., and W. H. Schubert, 2009: Rapid development of the tropical cyclone warm core. *J. Atmos. Sc.*, **66**, 3335–3350, doi:10.1175/2009JAS3092.1.

Wang, Y., 2012: Recent research progress on tropical cyclone structure and intensity. *Tropical cyclone Res. Rev*., **1**, 254–275. doi:10.6057/2012TCRR02.05.

Wang, Y., 2015: Hurricane Dynamics. *Encyclopedia of Atmospheric Sciences*, 2nd edition, Vol. 6, 8–29, Gerald R. North (editor-in-chief), John Pyle and Fuqing Zhang (editors). Elsevier Ltd, doi:10.1016/B978-0-12-382225-3.00488-6.

Wang, Y., and J. Xu., 2010: Energy production, frictional dissipation, and maximum intensity of a numerically simulated tropical cyclone. *J. Atmos. Sci.*, **67**, 97–116, doi: 10.1175/2009JAS3143.1.

Wang, Y., Y. Li, J. Xu, Z.-M. Tan, and Y. Lin, 2021a: The intensity-dependence of tropical cyclone intensification rate in a simplified energetically based dynamical system model. *J. Atmos. Sci*., **78**, 2033–2045, doi: 10.1175/JAS-D-20-0393.1.

Wang, Y., Y.-L. Li, and J. Xu, 2021b: A new time-dependent theory of tropical cyclone intensification. *J. Atmos. Sci.*, **78**, 3855–3865, doi:10.1175/JAS-D-21-0169.1

Xu, J., and Y. Wang, 2015: A statistical analysis on the dependence of tropical cyclone intensification rate on the storm intensity and size in the North Atlantic. *Wea. Forecasting*, **30**, 692–701, doi:10.1175/WAF-D-14-00141.1.

Xu, J., Y. Wang, and Z.-M. Tan, 2016: The relationship between sea surface temperature and maximum potential intensification rate of tropical cyclones over the North Atlantic. *J. Atmos. Sci.*, **73**, 4979–4988, doi: 10.1175/JAS-D-16-0164.1.

Xu, J., and Y. Wang, 2018a: Dependence of tropical cyclone intensification rate on sea surface temperature, storm intensity, and size in the western North Pacific. *Wea. Forecasting*, **33**, 523–537, doi:10.1175/WAF-D-17-0095.1.

Xu, J., and Y. Wang, 2018b: Effects of the initial vortex structure on intensification of a numerically simulated tropical cyclone. *J. Meteor. Soc. Japan*, **96**, 111–126, doi: 10.2151/jmsj.2018-014.

Xu, J., Y. Wang, and C. Yang, 2019a: Factors affecting the variability of maximum potential intensity (MPI) of tropical cyclones over the North Atlantic. *J. Geophys. Res.: Atmos.,* **124**, 6654–6668. doi:10.1029/2019JD030283.

Xu, J., Y. Wang, and C. Yang, 2019b: Interbasin differences in the median and variability of tropical cyclone MPI in the northern hemisphere. *J. Geophys. Res.: Atmos.*, **124**, 13,714–13,730, doi:10.1029/2019JD031588.

Zhang, J. A., R. F. Rogers, D. S. Nolan, F. D. Marks, 2011: On the characteristic height scales of the hurricane boundary layer. *Mon. Wea. Rev.*, **139**, 2523–2535, doi:10.1175/MWR-D-10-05017.1.

Zhang, J. A., R. F. Rogers, D. S. Nolan, and F. D. Marks, 2011: On the characteristic height scales of the hurricane boundary layer. *Mon. Wea. Rev.*, **139**, 2523–2535, doi:10.1175/MWR-D-10-05017.1.

Table 1. List of basic information about TC sample size and the intensification cases in each basin considered in this study.

Basin	TC numbers	Intensification cases
North Atlantic	362 (24.2%)	2885 (24.5%)
Western North Pacific	591 (39.5%)	5167 (44.0%)
Central and eastern North Pacific	543 (36.3%)	3706(31.5%)
Total	1496	11758

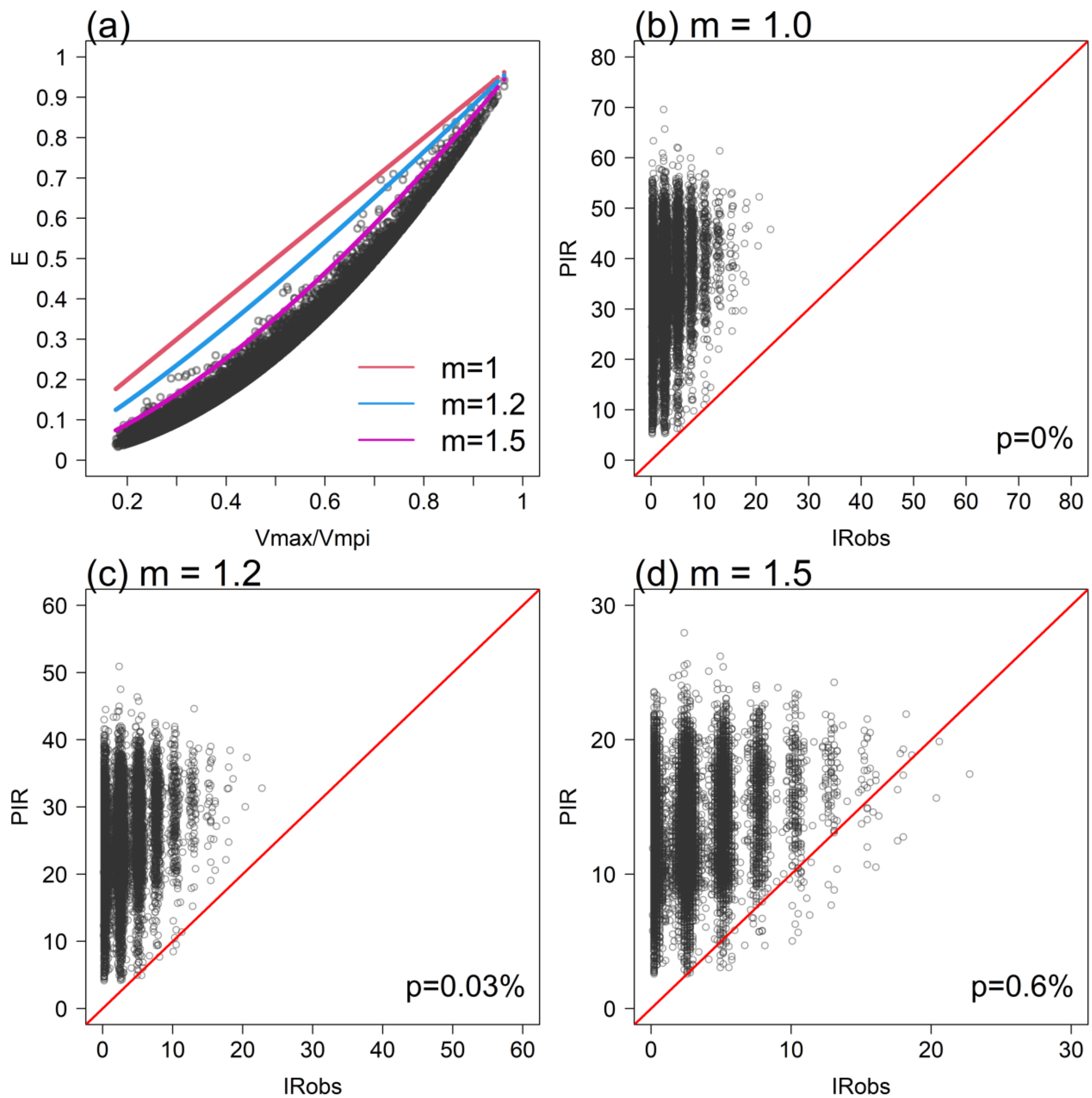

Figure 1. Scatter diagrams of *E* estimated from observations against relative intensity (Vmax/Vmpi) based on Eq. (1), together with *m* = 1 (red), *m* = 1.2 (blue), and *m* = 1.5 (purple) for *E** from Eq. (5) based on the best-track dataset (a), the theoretical PIR [m s^{-1} $(6h)^{-1}$] calculated with (b) *m* = 1, (c) *m* = 1.2, and (d) *m* = 1.5, respectively, against observed IR [m s^{-1} $(6h)^{-1}$]. Solid lines in (b-d) denote for y=x and percentage value on the right bottom gives percentage of the case numbers of theoretical PIR less than that of observed IR.

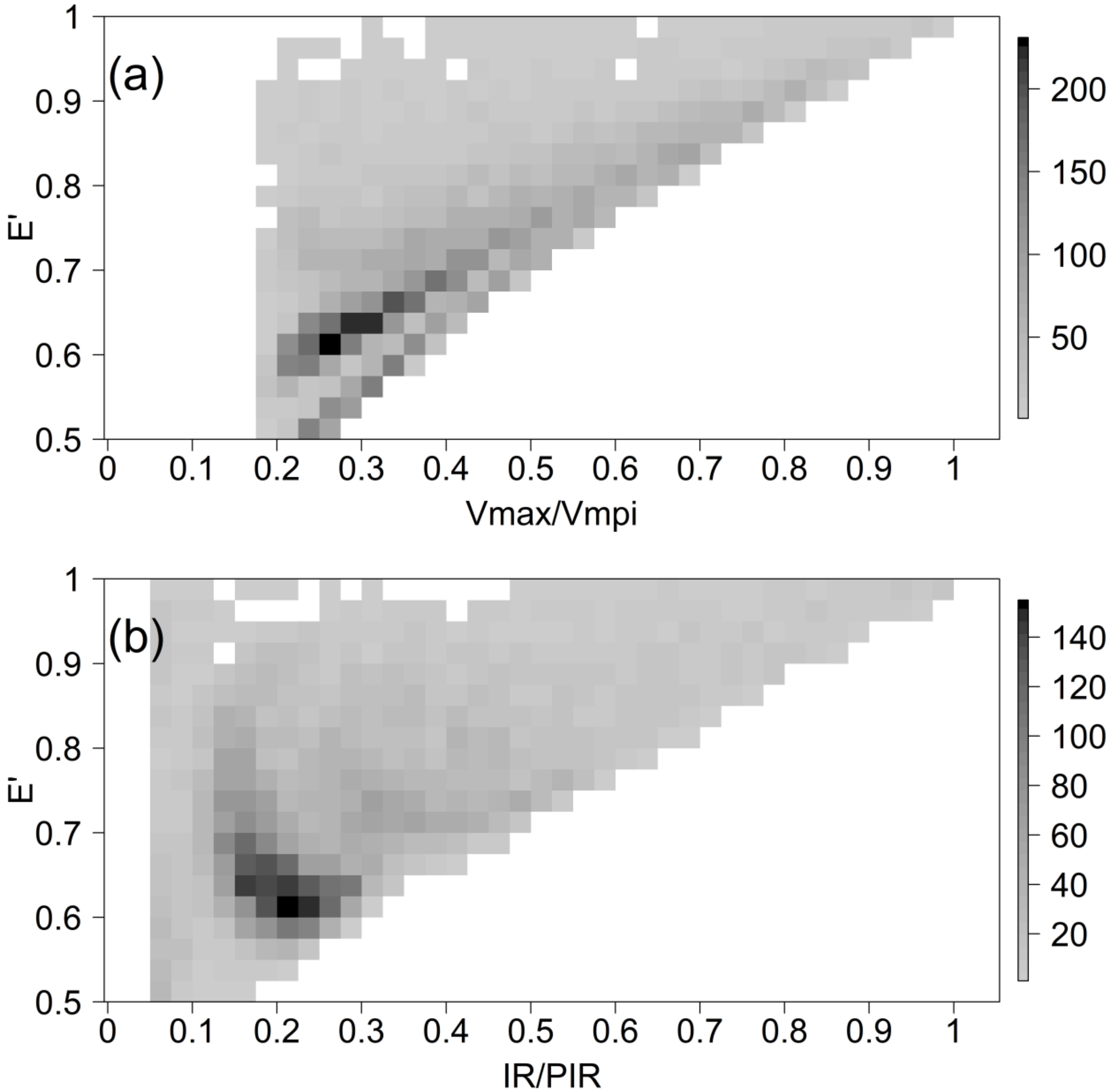

Figure 2. The 2-D histogram of the environmental dynamical efficiency (E') and (a) the relative intensity (V_{max} / V_{mpi}), and (b) the relative IR (namely IR normalized by the theoretical PIR) .

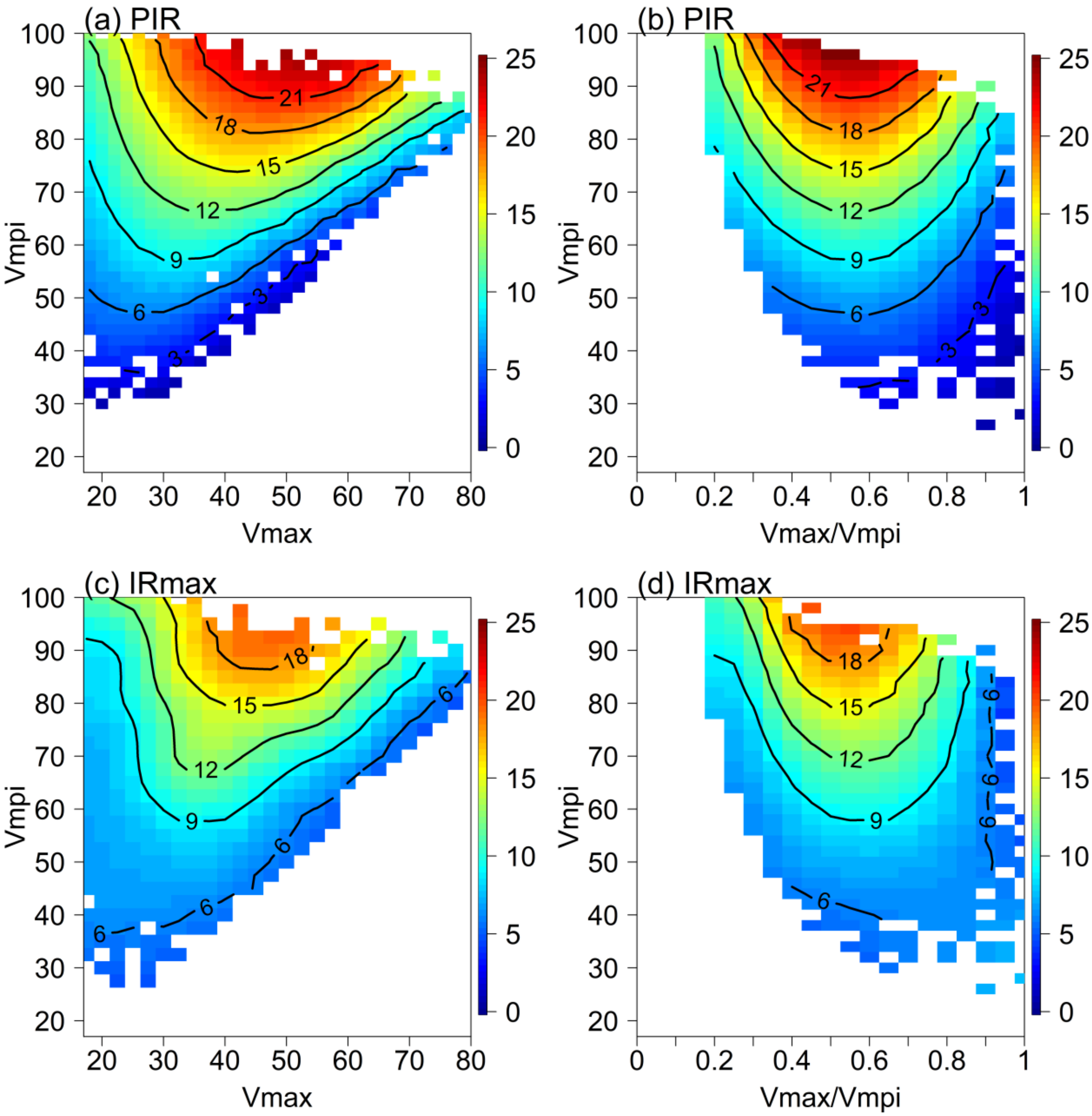

Figure 3. Distribution of TC theoretical PIR [m s^{-1} (6h)$^{-1}$] as a function of MPI (V_{mpi}, m s^{-1}) and (a) V_{max} (m s^{-1}) and (b) relative intensity (V_{max} / V_{mpi}) , respectively, (c) ~ (d) are same as (a) ~ (b), but for the 99th percentile of the observed IRs [m s^{-1} (6h)$^{-1}$].

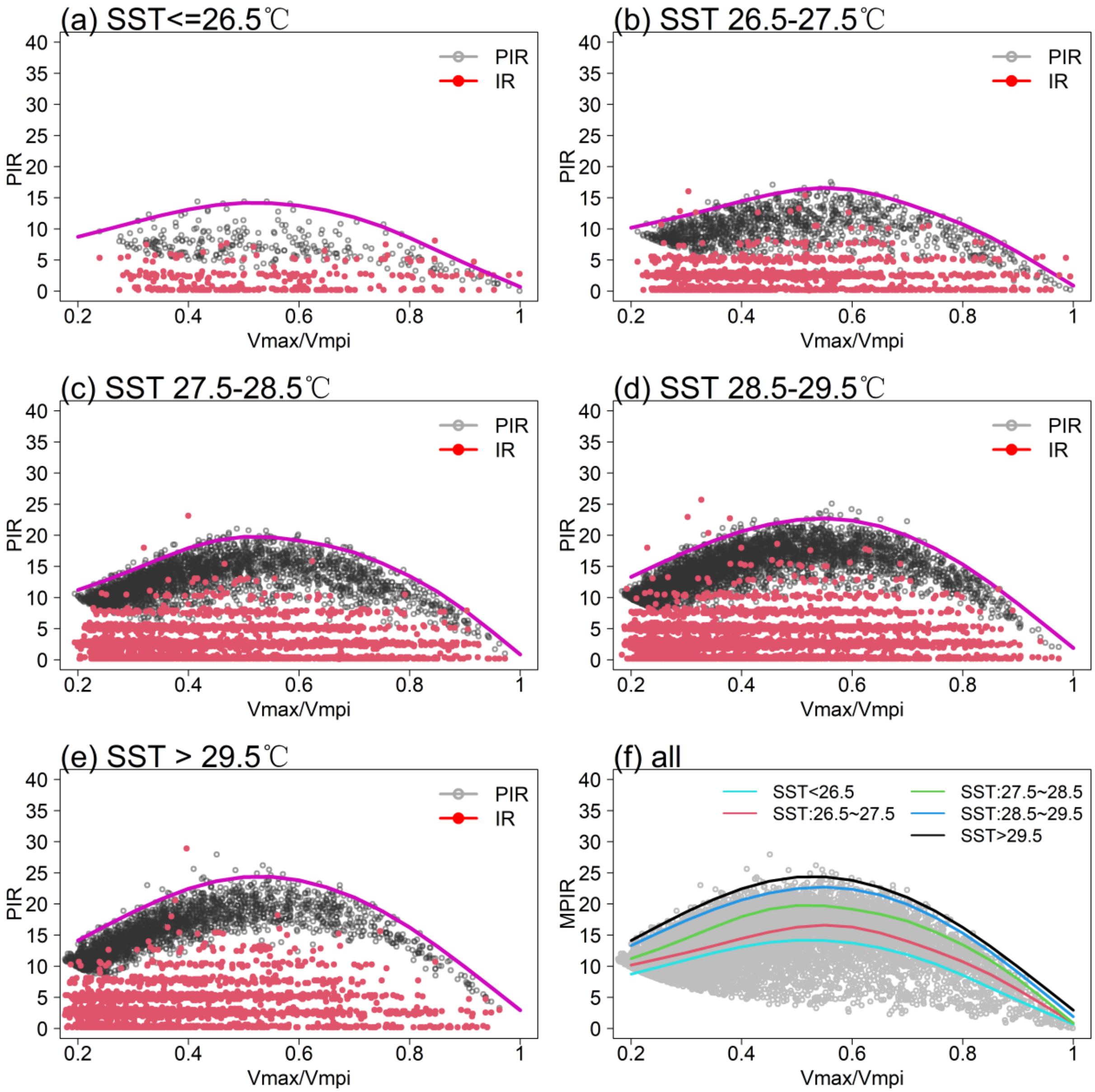

Figure 4. (a) – (e) show the Scatter diagram of TC PIR [dark grey, m s^{-1} $(6h)^{-1}$], and observed IR [red, m s^{-1} $(6h)^{-1}$] against relative intensity, with the 99th percentile of PIR fitted by non-parametric quantile regression for different SST bins (purple solid). The 99th percentile of theoretical PIR (solid) and PIR dots of each SST bins are shown together in (f).

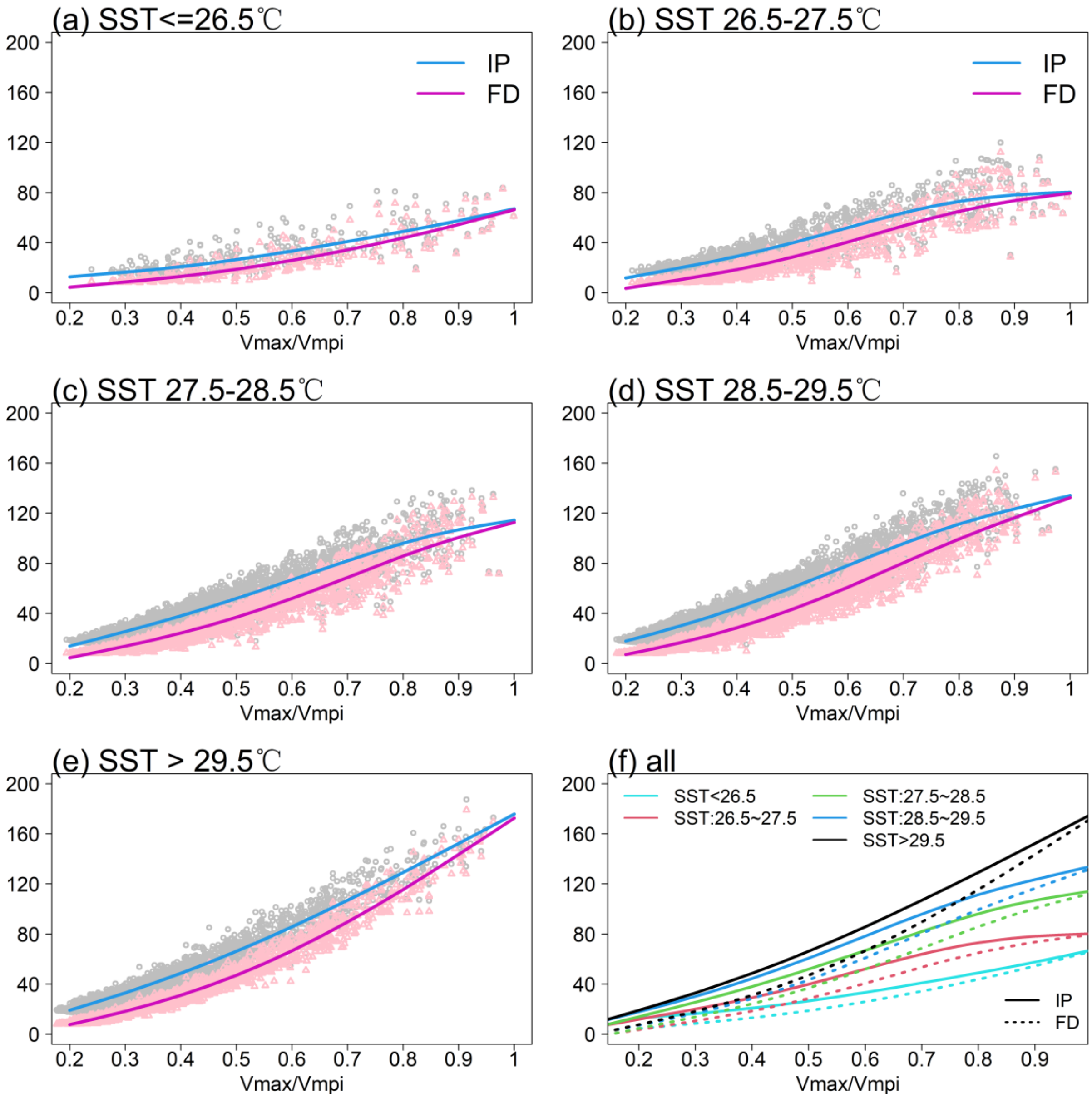

Figure 5. Scatter diagram of intensification potential [m s^{-1} (6h)$^{-1}$, grey] and frictional weakening rate [m s^{-1} (6h)$^{-1}$, pink] against relative intensity for all intensifying TC cases in various SST bins (a ~ e). The medians of IP and FD are given in blue, purple solid curves, respectively. The corresponding medians for each SST bin are also shown in (f) for a comparison.